ADVANCES IN ATMOSPHERIC SCIENCES, VOL. 28, NO. 1, 2011, 80–98

Water Vapor and Cloud Radiative Forcings over the Pacific Ocean Simulated by the LASG/IAP AGCM: Sensitivity to Convection Schemes

WU Chunqiang[1,2] (吴春强), ZHOU Tianjun*[1] (周天军),
SUN De-Zheng[3] (孙德征), and BAO Qing[1] (包 庆)

[1] *The State Key Laboratory of Numerical Modeling for Atmospheric Sciences and Geophysical Fluid Dynamics, Institute of Atmospheric Physics, Chinese Academy of Sciences, Beijing* 100029

[2] *National Satellite Meteorological Center, China Meteorological Administration, Beijing* 100081

[3] *Cooperative Institute for Environmental Studies/University of Colorado & Earth System Research Laboratory/NOAA, Boulder, Colorado, USA*

(Received 24 November 2009; revised 17 May 2010)

ABSTRACT

Characteristics of the total clear-sky greenhouse effect (GA) and cloud radiative forcings (CRFs), along with the radiative-related water vapor and cloud properties simulated by the Spectral Atmospheric Model developed by LASG/IAP (SAMIL) are evaluated. Impacts of the convection scheme on the simulation of CRFs are discussed by using two AMIP (Atmospheric Model Inter-comparison Project) type simulations employing different convection schemes: the new Zhang–McFarlane (NZH) and Tiedtke (TDK) convection schemes. It shows that both the climatological GA and its response to El Niño warming are simulated well, both in terms of spatial pattern and magnitude. The impact of the convection scheme on GA is not significant. The climatological longwave CRF (LWCRF) and its response to El Niño warming are simulated well, but with a prominently weaker magnitude. The simulation of the climatology (response) of LWCRF in the NZH (TDK) run is slightly more realistic than in the TDK (NZH) simulation, indicating significant impacts of the convection scheme. The shortwave CRF (SWCRF) shows large biases in both spatial pattern and magnitude, and the results from the TDK run are better than those from the NZH run. A spuriously excessive negative climatological SWCRF over the southeastern Pacific and an insufficient response of SWCRF to El Niño warming over the tropical Pacific are seen in the NZH run. These two biases are alleviated in the TDK run, since it produces vigorous convection, which is related to the low threshold for convection to take place. Also, impacts of the convection scheme on the cloud profile are discussed.

Key words: SAMIL, convection scheme, cloud radiative forcing, greenhouse effect

Citation: Wu, C. Q., T. J. Zhou, D.-Z. Sun, and Q. Bao, 2011: Water vapor and cloud radiative forcings over the Pacific Ocean simulated by the LASG/IAP AGCM: Sensitivity to convection scheme. *Adv. Atmos. Sci.*, **28**(1), 80–98, doi: 10.1007/s00376-010-9205-1.

1. Introduction

Water vapor and clouds play vital roles in the radiative, heat, and hydrologic budgets of the earth–atmosphere system, both of which constitute a major feedback mechanism in the climate system. Water vapor feedback is the largest positive feedback mechanism, and cloud feedback is found to provide the largest source of uncertainty in the climate sensitivity of current climate models (Colman, 2003; Soden and Held, 2006). It has been recognized for decades that these feedback mechanisms influence greatly the

*Corresponding author: ZHOU Tianjun, zhoutj@lasg.iap.ac.cn

mean state, seasonal cycle, and interannual variations of climate (Hall and Manabe, 1999; Sun et al., 2003; Guilyardi et al., 2009; Lloyd et al., 2009). However, it has been a big challenge for the current state-of-the-art climate models to reproduce them reasonably (Cess et al., 1990, 1996; Sun et al., 2006; Randall et al., 2007).

The convection scheme is at the core of climate modeling (Arakawa, 2004). The high sensitivity of the modeled atmosphere to the parameterization of deep convection has been documented in a number of studies (Zhang and McFarlane, 1995; Emanuel and Zivkovic-Rothman, 1999; Maloney and Hartmann, 2001; Song et al., 2008; Chen et al., 2010). The parameterizations of convection and the associated clouds act to mimic the way in which the atmosphere is destabilized by surface heating, and how its properties are mixed vertically. The formation of clouds, which is a major conditioner for atmospheric radiation, depends on the distributions of humidity and atmospheric stability. Hourdin et al. (2006) presented the impacts of the convection scheme on the vertical distributions of convective heating, moistening, and cloud amount and suggested that changing the convection scheme has a dominant impact on cloud formation compared to the cumulus cloud scheme in the Institute Pierre Simon Laplace (IPSL) AGCM. Also, impacts of the convective scheme on radiation through modifying the cloud water path and column precipitable water have been discussed carefully (Li and Zhang, 2008; Li et al., 2009).

In the State Key Laboratory of Numerical Modeling for Atmospheric Sciences and Geophysical Fluid Dynamics (LASG), Institute of Atmospheric Physics (IAP), great effort has been devoted to the development of climate system models [see Zhou et al., 2007 for a review]. The LASG/IAP model has been involved in both past climate simulation and future climate projection activities organized by the World Climate Research Program Coupled Model Inter-comparison Project (WCRP CMIP) for the Intergovernmental Panel on Climate Change (IPCC) Fourth Assessment Report (AR4) and many other international projects (Zhou et al., 2005a; Zhou and Yu, 2006; Li et al., 2007; Yu et al., 2008; Sanchez-Gomez et al., 2008; Zhou et al., 2009a, 2009b, 2009c; Scaife et al., 2009; Kucharski et al., 2009; Hodson et al., 2010; Li et al., 2010a, b). The AGCM is the core component of the fully coupled model (Wen et al., 2007; Zhou et al., 2008), and improvements in the LASG/IAP spectral AGCM have been made recently (Bao et al., 2010). Li et al. (2009) evaluated the impacts of the radiation scheme and convection scheme on the energy balance at the top-of-atmosphere and at the surface. Recently, observed precipitation over tropical regions and the vertical structure of temperature anomalies associated with El Niño simulated by the Spectral Atmospheric Model developed by the LASG/IAP (SAMIL), as well as their sensitivity to the choice of convection scheme have been examined carefully (Liu et al., 2007; Zhang et al., 2010a). However, less attention has been paid to the impacts of the convection scheme on simulations of radiative forcings associated with water vapor and clouds in SAMIL.

The main motivation for this study is to measure the reliabilities of the simulated total clear-sky greenhouse effect (GA) and cloud radiative forcings (CRFs) by SAMIL, and to discuss the impacts of convection scheme choice on the simulation of GA and CRFs. Responses of GA and CRFs to El Niño forcing are also examined.

The remainder of the paper is organized as follows. We describe the model, observational data, and methodology in section 2. In section 3, the climatological GA and CRFs simulated by the model are compared against observations. The responses of GA and CRFs to El Niño warming are discussed in section 4, and a brief summary is presented in section 5.

2. Model description, data and methods

2.1 *Model description*

The SAMIL used in this study was a new version of the spectral AGCM developed by the LASG/IAP. It is rhomboidally truncated at zonal wave number 42, corresponding to a horizontal resolution of about 2.81° lon×1.66° lat, and has 26 vertical layers with a top of 2.1941 hPa. The cloud amount is calculated based on a diagnostic slingo-type scheme (Slingo, 1987) modified by Dai et al. (2005). In Dai et al. (2005), the low level cloud amount is diagnosed based on the observational statistical relationship between low level cloud amount and low troposphere stability. In SAMIL, the Xu and Randall (1996) scheme is employed, in which the cloud droplet effective radius is diagnosed based on the cloud water/ice mixing ratio and temperature. The cloud water/ice mixing ratio and temperature are highly correlated to the convection scheme used. Compared with its predecessors, this new version of SAMIL uses a new radiation scheme developed by Edwards and Slingo (1996) and modified by Cusack et al. (1998) and Sun (2005); namely, SES2. Also, the non-local boundary layer scheme of Holtslag and Moeng (1991) is used in this model. Further information regarding the model can be found in Zhou et al. (2005a, b). The model has been widely used in monsoon studies (Zhang et al., 2010b).

Two different convection schemes are employed in SAMIL: the new Zhang–McFarlane convection scheme (Zhang, 2002) and the Tiedtke convection scheme (Tiedtke, 1989) modified by Nordeng (1994) and Song (2005). The original Zhang–McFarlane scheme is based on a plume ensemble approach, which assumes that an ensemble of convective scale updrafts (and the associated saturated downdrafts) may exist whenever the atmosphere is conditionally unstable in the lower troposphere (Zhang and McFarlane, 1995). The new Zhang–McFarlane scheme, which is employed in SAMIL, differs from the original version in its closure assumptions (Zhang, 2002). The original scheme assumes that convection removes the atmospheric convective available potential energy with a relaxation timescale of a few hours, and the cloud base mass flux is proportional to the amount of convective instability in the atmosphere. The new closure assumes that convection only responds to forcing from large-scale processes in the free troposphere above the boundary layer. It is not directly related to the amount of convective instability, and only requires the atmosphere to be convectively unstable. In addition, since only the deep convection is parameterized by the Zhang–McFarlane scheme, the Hack scheme (Hack, 1994) is employed to prescribe the shallow convective processes.

The Tiedtke convection scheme is a bulk flux convection scheme (Tiedtke, 1989). It handles three types of convection: deep, middle level, and shallow convection. In the Tiedtke scheme, only one convective cloud is considered, comprising one single saturated updraft. Entrainment and detrainment between the cloud and the environment can take place at any level between the free convection level and the zero-buoyancy level. There is also one single downdraft extending from the free sinking level to the cloud base. The mass flux at the top of the downdraft is a constant fraction (here 0.3) of the convective mass flux at the cloud base. This downdraft is assumed to be saturated and is kept at saturation by evaporating precipitation. The original closure assumption for deep convection relies on a closure in moisture convergence, while that used in this version is based on the convective available potential energy (CAPE) modified by Nordeng (1994). Also, the cloud top height and organized outflow identified by the Tiedtke scheme were modified by Song (2005).

In this study, two AMIP (Atmospheric Model Intercomparison Project) type simulations, one using the new Zhang–McFarlane convection scheme (hereafter NZH) and one employing the Tiedtke convection scheme (hereafter TDK), were conducted. The SAMIL model is forced by historical SST data spanning the period of 1976–1999. However, only the results from

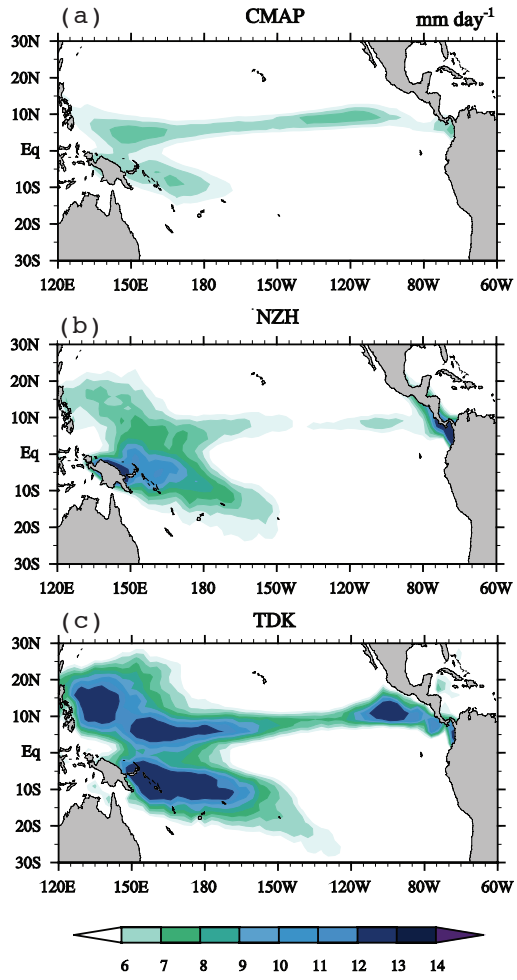

Fig. 1. Geographical distributions of annual mean precipitation from (a) CMAP data; (b) simulation using NZH; and (c) simulation using TDK over the period 1985–1999. Units: mm d^{-1}.

1984–1999 were used in this analysis. The tropical climate is reproduced well by SAMIL. Figure 1 shows climatological precipitation from the CPC (Climate Prediction Center) Merged Analysis of Precipitation (CMAP) dataset (Xie and Arkin, 1997) and from two simulations. The two simulations captured the spatial pattern of annual mean precipitation. However, the magnitudes of precipitation in the two simulations were overestimated compared to the CMAP data. Compared to the simulation using NZH, the precipitation in the simulation using TDK was more abundant, indicating that the convection in TDK is more vigorous than that in NZH. In addition, the precipitation characteristics over the East Asian domain are simulated well to a certain extent as many other AGCMs (Zhou and Li, 2002; Chen et al., 2009; Bao et al., 2010).

2.2 *Observational data*

The observational data used in this study consisted of: (1) observed radiative fluxes at the top-of-atmosphere (TOA) from the International Satellite Cloud Climatology Project (ISCCP) FD (flux D series) monthly data (Zhang et al., 2004), which are calculated based on the ISCCP 3 hourly D series data (D1) cloud data (Rossow and Schiffer, 1999) and widely used in climate research (Bony and Dufresne, 2005; Collins et al., 2006; Schmidt et al., 2006); (2) cloud information from the ISCCP monthly D series data (D2) gridded monthly data (Rossow and Duenas, 2004), which includes the total cloud amount as well as high, middle, and low level cloud amounts; (3) The specific humidity and vertical velocity from European Center for Medium-Range Weather Forecasts (ECMWF) 40-year reanalysis (ERA-40) (Uppala, 2006); (4) the observed SST from Smith and Reynolds (2004) and (5) the precipitation from CPC Merged Analysis of Precipitation (CMAP, Xie and Arkin, 1997).

2.3 *Analysis method*

In our analysis, total clear-sky greenhouse radiative forcing (GA) at TOA was quantified as in Raval and Ramanathan (1989):

$$\mathrm{GA} = \sigma T_{\mathrm{s}}^4 - F_{\mathrm{clear}} \ , \tag{1}$$

where σ is the Stefan-Boltzmann constant, and T_{s} denotes SST. We assumed the surface emissivity to be unity since only oceanic regions are of concern in this study. F_{clear} represents the upward clear-sky longwave flux at TOA.

Following Charlock and Ramanathan (1985), the longwave and shortwave CRFs (LWCRF and SWCRF, respectively) at TOA were defined as:

$$\mathrm{LWCRF} = F_{\mathrm{clear}} - F \ ; \tag{2}$$

$$\mathrm{SWCRF} = S - S_{\mathrm{clear}} \ . \tag{3}$$

In the above equations, F_{clear} and F represent the upward clear-sky and all-sky longwave flux at TOA, respectively. S_{clear} and S are the clear-sky and all-sky net downward solar radiation fluxes at TOA, respectively.

The responses of GA and CRFs to El Niño warming were examined using the regression analysis technique used by Sun et al. (2003). Using the observed variation of SST anomalies averaged over the Pacific cold-tongue region (5°S–5°N, 150°E–110°W) on the interannual timescale as an index, the response of GA and CRFs were quantified by regressing linearly the corresponding components to the SST anomaly (SSTA) index.

Table 1. Annual mean GA, LWCRF, and SWCRF averaged over the low- and middle-latitude Pacific Ocean (60°S–60°N, 100°E–80°W) during the period 1985–1999. ISCCP radiative data (Zhang et al., 2004) is taken as the observational evidence. NZH and TDK stand for simulations using the new Zhang–McFarlane (Zhang, 2002) and Tiedtke (Tiedtke, 1989) convection scheme respectively.

	Forcing (W m^{-2})		
	GA	LWCRF	SWCRF
ISCCP	149.9	27.7	−59.1
NZH	146.9	15.4	−50.5
TDK	147.2	27.6	−64.5

3. Evaluation of climatology

3.1 *GA*

GA is a dominant positive radiative forcing in the climate system and a potential amplifier of global warming (Houghton et al., 2001). The annual mean GA averaged over the Pacific Ocean (60°S–60°N, 100°E–80°W) in the ISCCP data and the two simulations (i.e. using NZH and TDK) are listed in Table 1. The annual and regional mean GA in the ISCCP data is about 149.9 W m^{-2}. The model estimate results are close to those from the ISCCP data, with a negative bias of 3.0 (2.6) W m^{-2} for the simulation using NZH (TDK), which is less than 2% of the observed value and is within the scope of observational uncertainty since the uncertainty in the monthly and global averaged GA is about 5–10 W m^{-2} (Raval and Ramanathan, 1989), indicating reasonable model performances for both configurations.

The geographical distribution of the observed annual mean GA shows large values over convective regions, i.e. the western Pacific warm pool, the Intertropical Convergence Zone (ITCZ) and the South Pacific Convergence Zone (SPCZ), and small values over the cold water regions off California and Peru, together with a decrease from the equator to the poles (Fig. 2a). The two simulations reproduce this feature well (Figs. 2b and 2c), and spatial correlations between the two simulations and observed results from the ISCCP data over the Pacific Ocean both exceed 0.99, which are statistically significant at the 0.5% level. Spatially, the GA is underestimated (overestimated) by about 5–10 W m^{-2} at low (high) latitudes, and these differences are significant over the Pacific cold tongue region and high latitudes in both simulations. Generally, the differences between the two simulations are indiscernible in terms of the magni-

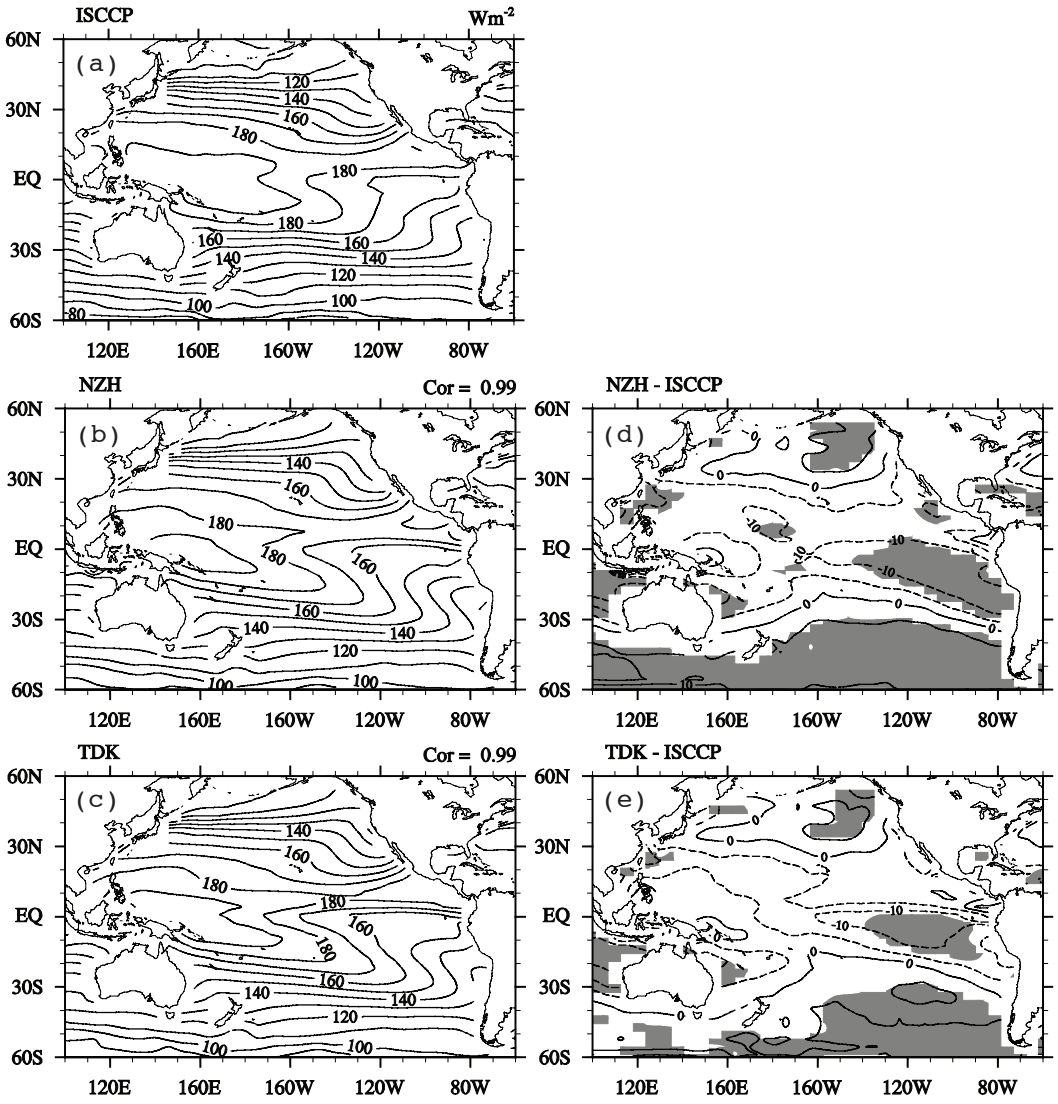

Fig. 2. Geographical distributions of annual mean GA from (a) ISCCP data; (b) simulation using NZH; and (c) simulation using TDK over the period 1985–1999. The numbers in the top-right corner of (b) and (c) denote the pattern correlations between the ISCCP data and the two simulations. The differences with respect to the ISCCP data are shown in (d) and (e) for the NZH and TDK simulations respectively, with differences significant at the 1% level being shaded. The contour interval is 10 W m^{-2}.

tude and spatial pattern of annual mean GA over the Pacific Ocean.

3.2 *CRFs*

Simulating CRFs and cloud structures, which are linked to one another, are difficult and therefore act as a rigorous test for climate models. From the ISCCP data, the annual mean LWCRF averaged over the Pacific Ocean is 27.7 W m^{-2} (Table 1). The estimate from the simulation using TDK (27.6 W m^{-2}) is close to the ISCCP value, while that of the simulation using NZH (15.4 W m^{-2}) is clearly an underestimation, about a half of the ISCCP value.

The horizontal distributions of the annual mean LWCRF from the ISCCP data and the two simulations over the Pacific Ocean are shown in Figs. 3a–3c. The LWCRF in the ISCCP data exhibits maximum centers over the western Pacific warm pool region and along the ITCZ and SPCZ, and minimum centers over the cold water regions (Fig. 3a). The spatial correlations between the two simulations and the ISCCP results are 0.64 and 0.75 for the simulations using NZH and TDK, respectively (Figs. 3b and 3c). Even though these correlation coefficients pass the 1% statistical significance level, the differences in magnitude between the observed (ISCCP) and modeled LWCRFs are ob-

vious (Figs. 3d and 3e), especially in the simulation using NZH. As seen from the difference map, the annual mean LWCRF is underestimated over the strong convective regions, i.e. the western Pacific warm pool, ITCZ, as well as the SPCZ, and overestimated over the Pacific cold tongue region and the middle and high latitudes in the simulation using TDK (Fig. 3e). The differences between the simulation using TDK and the ISCCP data over most areas of the Pacific Ocean are within 10 W m^{-2} and are not significant. The annual mean LWCRF over the Pacific Ocean is degraded in the simulation using NZH compared to that using TDK. The annual mean LWCRF is underestimated over almost the entire Pacific Ocean, with maximum difference centers of up to 30 W m^{-2} along the ITCZ and SPCZ, and the differences over most regions being statistically significant at the 0.5% level.

Even though the upper level cloud amount has been proposed to be a dominant factor influencing the outgoing longwave radiation (OLR) at the TOA (Ockert-Bell and Hartmann, 1992a, 1992b), the discrepancy in LWCRF can hardly be attributed to the bias in the upper level cloud amount. Our results based on the ISCCP data and the two simulations show that both the temporal and spatial correlations between LWCRF and upper level cloud amount are statistically significant at the 0.5% level and are much higher than that between LWCRF and total cloud amount or middle/low level cloud amount, indicating a connection between high level cloud amount and LWCRF. However, the high level cloud amount is unlikely to be responsible for the underestimation in LWCRF, since it is overestimated in both simulations (Fig. 4b and 4c). In the NZH simulation, it is overestimated over the whole region, especially over the western North Pacific (Fig. 4b), where it is overestimated by more than 20%. The TDK run has an even larger bias and overestimates the high level cloud

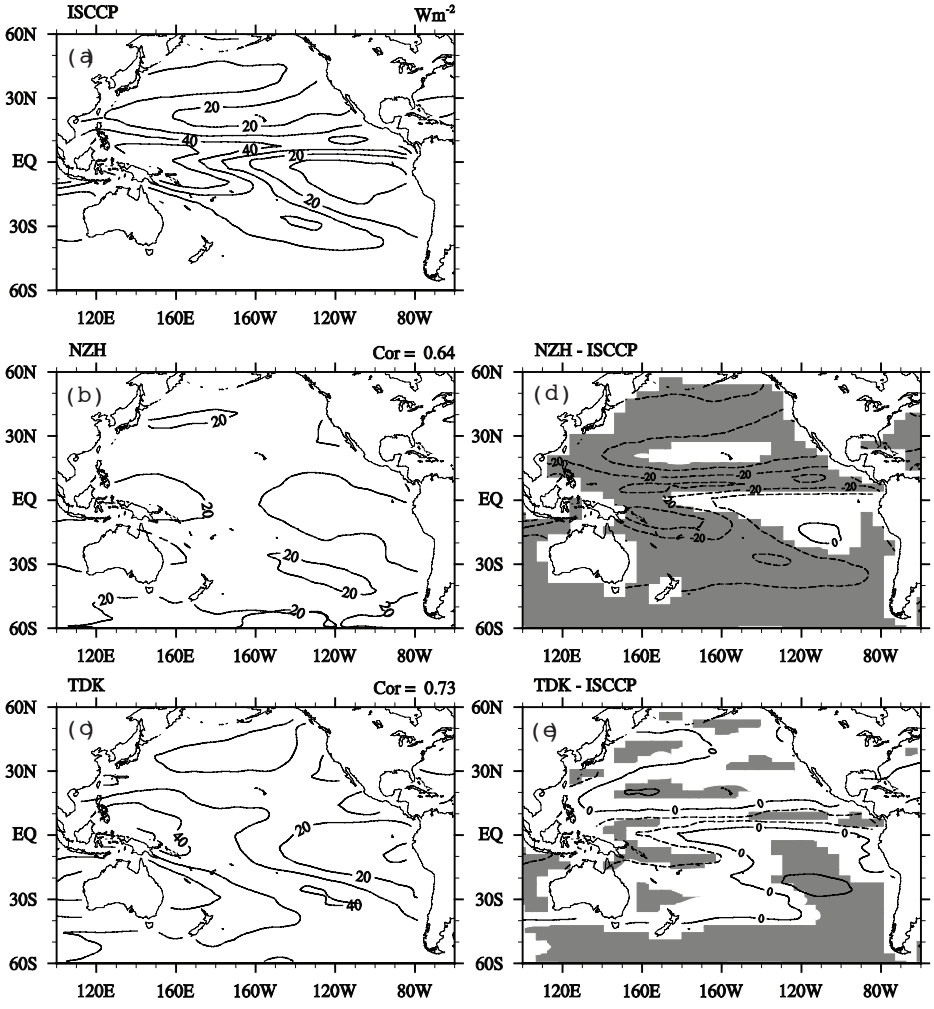

Fig. 3. As in Fig. 2 except for LWCRF.

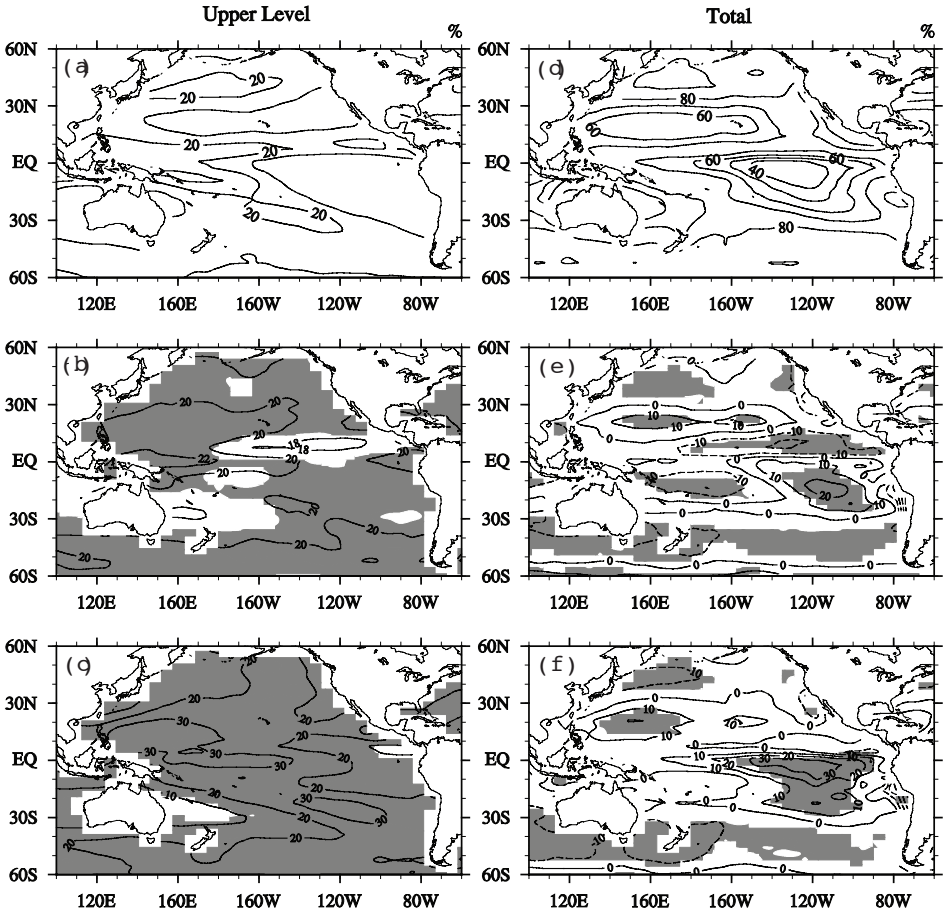

Fig. 4. Geographical distributions of (a) annual mean upper-level cloud amount from the ISCCP data and the difference of annual mean total cloud amount between (b) the NZH and (c) TDK simulations and the ISCCP data. (d)–(f): Same as (a)–(c), except for the total cloud amount. The differences which are statistically significant at the 1% level are shaded. The contour interval is 10%.

amount by 40% over the northwestern Pacific Ocean (Fig. 4c). This overestimation is a common issue for many AGCMs whose cloud amount is empirically related to relative humidity and, possibly, precipitation (Weare and Groups, 1996).

The cloud ice water path is a cloud property that influences LWCRF (Shi, 2007), and a possible contributor to the bias in LWCRF. The cloud ice water paths from the two simulations were compared to the ISCCP data (Figs. 5a–5c). It can be seen that the cloud ice water path in the two simulations are underestimated over the ITCZ and the western Pacific warm pool region and overestimated over the subtropical ocean. To the first order, the spatial pattern of bias in the cloud ice water path is consistent with that of LWCRF, indicating that bias in the cloud ice water path could partly account for the discrepancy in LWCRF. The size of the cloud ice water path influences the emissivity of the high troposphere. The cloud ice water path in the TDK simulation is larger than that in the simulation using NZH. For example, the cloud ice water path over the western Pacific warm pool region in the TDK and NZH simulations are 40 mg m^{-2} and 20 mg m^{-2}, respectively. A larger cloud ice water path may be related to the strong convection presented by the Tiedtke scheme (Hourdin et al., 2006). The differences in LWCRF and related cloud properties between the NZH and TDK simulations confirm the notion that the type of convection scheme has an impact on results.

The annual mean SWCRF averaged over the Pacific Ocean is about -59.1 W m^{-2} in the ISCCP data, and the corresponding estimates from the NZH (TDK) simulations are -50.5 (-64.5) W m^{-2} (Table 1). This demonstrates that SWCRF is underestimated (overestimated) by the simulation using NZH (TDK) and the discrepancy in the NZH simulation is slightly stronger than in the TDK simulation.

The spatial patterns of annual mean SWCRF are

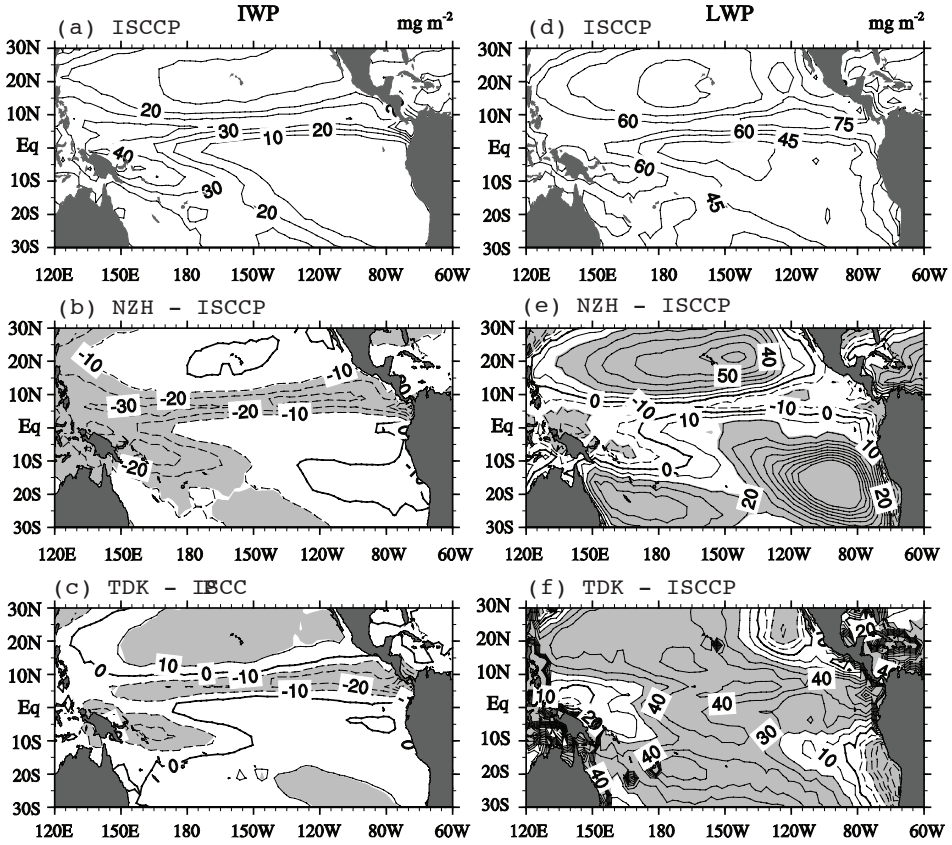

Fig. 5. As in Fig. 4 except for the cloud ice water path (a–c; IWP) and the cloud liquid water path (d–f; LWP). The differences which are statistically significant at the 1% level are shaded. The contour interval is 10 mg m^{-2} for both IWP and LWP.

presented in Fig. 6. In the tropics, the spatial pattern of SWCRF in the ISCCP data resembles that of LWCRF of the opposite sign, except that SWCRF shows larger values over the coasts off California and Peru. Additionally, there are larger values over the high latitude oceans (Fig. 6a). The spatial correlations between the two simulations and the ISCCP data are 0.04 and 0.26 for the simulations using NZH and TDK respectively (Fig. 6b and 6c). The spatial correlation between the ISCCP data and the simulation using TDK is significant at the 1% level, indicating that, to a certain extent, the TDK simulation reproduces a similar spatial pattern to the observed (ISCCP) data. The simulation using NZH produces a totally different SWCRF pattern from observed, i.e. from the ISCCP data. Over the Pacific Ocean, estimates of SWCRF in the NZH simulation are broadly weak (strong) in the low and high (middle) latitudes compared to the ISCCP data, with a maximum discrepancy of about 30 (−90) W m^{-2} (Fig. 6d). The differences between the ISCCP data and the simulation using NZH are significant over most parts of the Pacific Ocean, and the estimate in the southeastern Pacific region is about three times larger than the observed, i.e. from the ISCCP data. The SWCRF in the simulation using TDK is overestimated (underestimated) in the middle (high) latitudes compared to the ISCCP data, with a maximum discrepancy of about 10 (−20) W m^{-2} (Fig. 6e). The difference between the ISCCP data and TDK simulation is significant over the middle latitudes and some parts of the high latitudes over the Pacific Ocean. Besides the overestimation of SWCRF over the southeastern Pacific, another common bias in the two simulations is an underestimation of SWCRF over the coasts off California and Peru, where marine stratus is prevalent (Klein and Hartmann, 1993).

The discrepancy in SWCRF, to a large extent, can be related to the bias in total cloud amount. The annual mean total cloud amount from the ISCCP data and the differences between the two simulations and the ISCCP data are presented in Figs. 4d–4f. Comparing Figs. 6e–6f and Figs. 4e–4f, it can be seen that the difference pattern of total cloud amount resembles well that of SWCRF, both of which are underestimated (overestimated) in the low and high (middle) latitudes in the NZH simulation and underestimated (overesti-

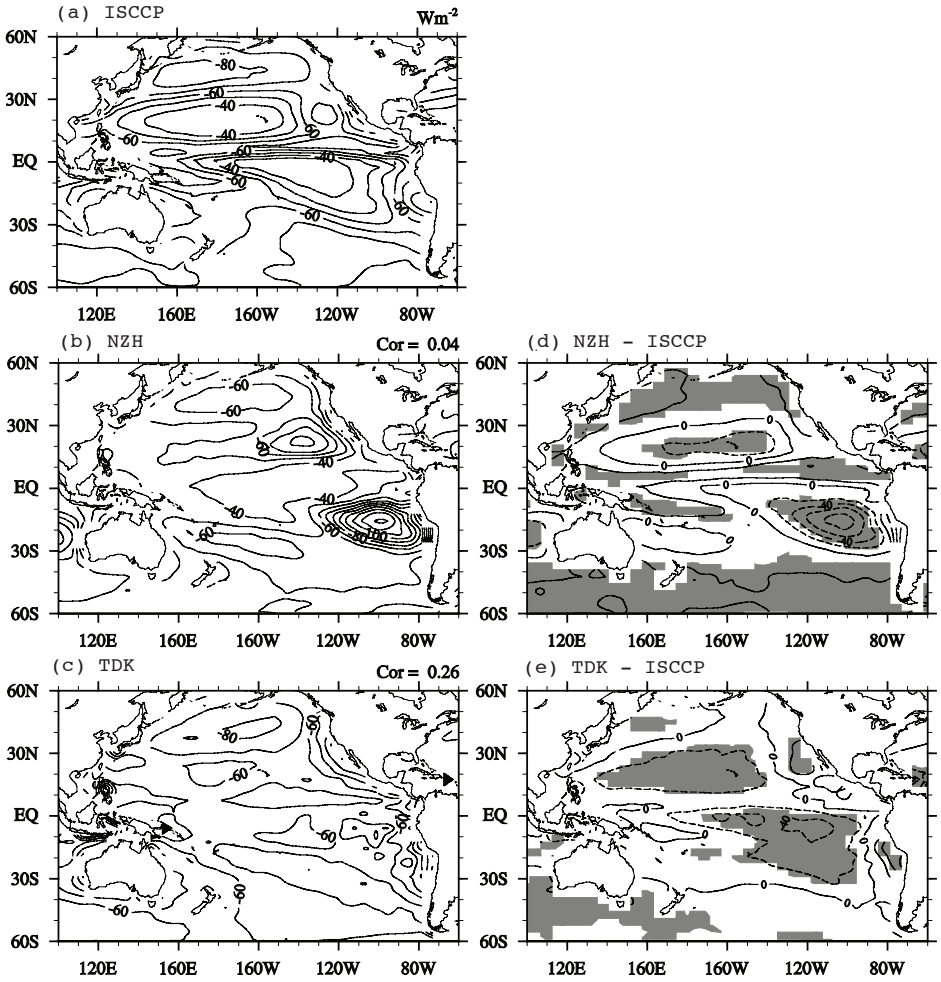

Fig. 6. As in Fig. 2 except for SWCRF. The contour interval is 10 W m^{-2} for (a)–(c) and 20 W m^{-2} for (d) and (e).

mated) in the high (middle) latitudes in the TDK run. This demonstrates that the total cloud cover biases are responsible for SWCRF biases in the two simulations.

The cloud water path is another factor that influences SWCRF, and may contribute to the bias in SWCRF, especially over the southeastern Pacific Ocean. The total cloud amount over the southeastern Pacific Ocean in the TDK simulation is larger than in the simulation using NZH (Fig. 4e and 4f), while the SWCRF in the simulation using TDK is less than in the NZH simulation (Fig. 6b and 6c). This difference is related to the cloud water path in the simulations (Figs. 5d–5f). The regional averaged (25°–10°S, 120°–80°W) column-integrated cloud water path is about 230 (110) mg m^{-2} for the NZH (TDK) simulation. This indicates that the column-integrated cloud water path is more than two times larger than that in the NZH simulation, which is consistent with the stronger SWCRF it yields. The size of the cloud water path is linked to the cloud profile, which is affected by the convection scheme. The NZH simulation exhibits one peak in the lower troposphere (below 900 hPa), while the TDK run shows two comparable peaks, one in the upper troposphere (around 250 hPa) and one in the lower troposphere (below 900 hPa), and the cloud amount in the lower troposphere in the TDK simulation is much smaller than in the simulation using NZH (Fig. 7). Since the cloud water path depends on the specific humidity, the NZH simulation has a larger cloud water path size. Considering the southeastern Pacific is characterized by subsidence motion, the TDK simulation may produce spuriously strong convection over this region.

4. Response to El Niño warming

Since there are of course no observational data available to verify cloud feedbacks in future climate

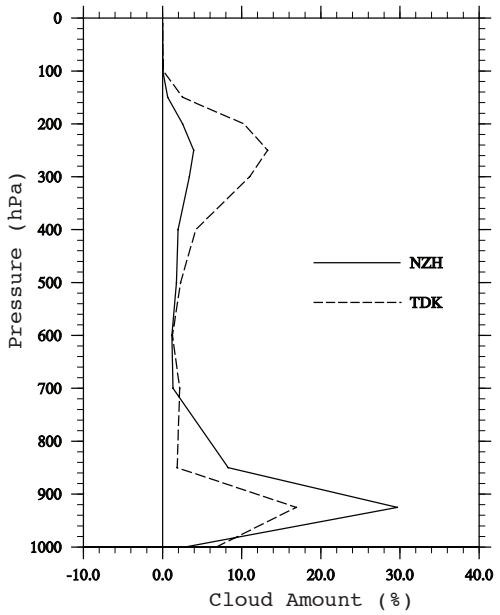

Fig. 7. The profiles of annual mean cloud amount averaged over the southeastern Pacific Ocean (25°–10°S, 120°–80°W) for the NZH and TDK simulations.

predicted by GCMs, a practical method to assess the climate sensitivity of clouds is to document the cloud variability associated with short-term climate anomalies observed in the current climate, such as the ENSO. The underlying philosophy is that if GCMs can actually predict long-term cloud–climate feedbacks, they must firstly be able to show a good ability to reproduce the cloud variations associated with climate anomalies occurring over shorter timescales. To quantify the feedbacks of GA and CRFs in response to El Niño warming, the methods of Sun et al. (2003) and Zhang and Sun (2006) were followed: linear regression coefficients of these components to underlying SST anomalies averaged over the tropical cold tongue region (5°S–5°N, 150°E–110°W) were calculated and are listed in Table 2.

4.1 *GA*

The observed GA response to El Niño warming is about 6.73 W m^{-2} K^{-1}, indicating that GA enhances as SST rises, constituting a positive feedback mechanism. These responses are overestimated by the two simulations, by about 20% (30%) in the simulation using NZH (TDK).

The spatial distributions of GA responses in the ISCCP data and the two simulations are illustrated in Figs. 8a–8c. In the ISCCP data, the response of GA to El Niño warming is characterized by a positive response along the equator, with a maximum center of about 12 W m^{-2} K^{-1} located in the central equatorial

Table 2. Responses of GA, LWCRF and SWCRF to El Niño warming averaged over the Pacific cold tongue region (5°S–5°N, 150°E–110°W) during the period 1985–1999. The observed radiation data is derived from the ISCCP retrieval (Zhang et al., 2004) and the SST data are from ERSST V2 (Smith and Reynolds, 2004). The error bars are obtained using the method of Press et al. (1992) for cases where measurement errors of individual data points are not known.

	Response (W m^{-2} K^{-1})		
	∂GA/∂T	∂LWCRF/∂T	∂SWCRF/∂T
ISCCP	6.73±0.28	11.69±0.96	−12.28±1.01
NZH	7.93±0.28	5.09±0.67	−4.56±0.48
TDK	8.72±0.44	5.94±0.78	−7.08±0.98

Pacific, and indiscernible responses over other parts of the tropical Pacific (Fig. 8a). This pattern is captured well by the two simulations, except with larger magnitudes (Fig. 8b and 8c); the maximum center of the NZH (TDK) run exceeds 14 (16) W m^{-2} K^{-1}. Also, the horseshoe-shaped negative responses around the positive response are both overestimated by the two simulations. Additionally, the TDK simulation overestimates the positive response over the southeastern Pacific region (Fig. 8c).

The bias in GA response could be attributable to the biases in the percentage responses of water vapor in the middle and upper troposphere (Zhang and Sun, 2008). The percentage responses of water vapor at 500 hPa are shown in Figs. 8d–8f, since the percentage changes in water vapor are more relevant to the changes in OLR (Shine and Sinha, 1991; Sun and Lindzen, 1993). The locations of the maximum responses of water vapor match well those of GA both in the reference data and the two simulations, all of which are located to the immediate east of the date line. Compared to the reference data, the percentage responses of water vapor are overestimated by both simulations, especially the TDK run, which overestimates the percentage response by more than 20% and is consistent with the bias in GA. In addition, the overestimation of GA in the TDK simulation over the southeastern Pacific corresponds well to the overestimation of water vapor there. However, although the response of water vapor is also overestimated over the eastern tropical Pacific in the NZH simulation, the response of GA in the NZH run is comparable to the reference data. This is partly due to error compensation between the response of water vapor and that of temperature; the response of temperature at 500 hPa to El Niño warming in the NZH simulation is stronger than in the ERA40 data (Zhang et al., 2010a). The contributions of high and low level water vapor were also examined. The discrepancies at high levels are

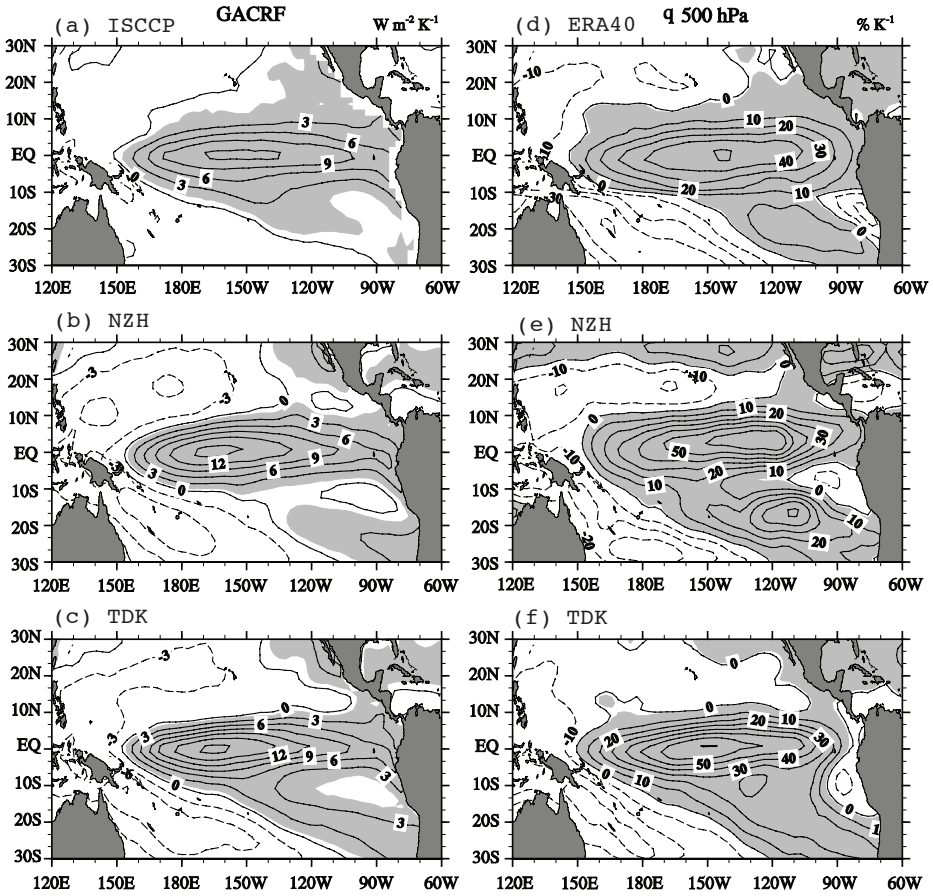

Fig. 8. Response of GA to El Niño warming from (a) ISCCP data; (b) simulation using NZH; and (c) simulation using TDK, and the percentage response of water vapor at 500 hPa from (d) ERA40 data; (e) simulation using NZH; and (f) simulation using TDK. Regression coefficients obtained by linearly regressing GA/water vapor at each grid point against the underlying SST averaged over the Pacific cold tongue region (5°S–5°N, 150°E–110°W) are shown. For water vapor, the regression coefficients of water vapor to the ENSO are divided by the climatology. The regression coefficients which are statistically significant at the 5% level are shaded. The contour interval is 3 W m^{-2} K^{-1} for (a)–(c) and 10% K^{-1} for (d)–(f).

similar to those at 500 hPa, while the discrepancies in the lower troposphere, such as at 850 hPa are relatively small (not shown). These results confirm that the bias in GA is caused by the bias in water vapor in the middle and high troposphere, where the water vapor is fed by the detrainment of the convection process (Del Genio and Kovari, 2002), highlighting the effect of the convection scheme on simulated GA.

4.2 *CRFs*

The LWCRF enhances with SST, and the response of LWCRF in the ISCCP data is about 11.69 W m^{-2} K^{-1}, while in the two simulations it is underestimated in both cases, at a value of 5.09 (5.94) W m^{-2} K^{-1} in the simulation using NZH (TDK). The response of LWCRF in the TDK run is slightly stronger than in the NZH simulation.

Horizontal patterns of LWCRF responses to El Niño warming are presented in Figs. 9a–9c. In the ISCCP data, the strong responses of LWCRF are restricted to the 10°S–10°N belt region, with a negative response over the maritime continent, and positive responses from the western-central tropical Pacific to the eastern tropical Pacific and a maximum positive response center over the central Pacific exceeding 20 W m^{-2} K^{-1} (Fig. 9a). The response over the eastern Pacific is asymmetrical to the equator, with the major response over the northern Pacific. The response pattern of LWCRF over the tropical Pacific is a reflection of the eastward shifts of precipitation and upper level

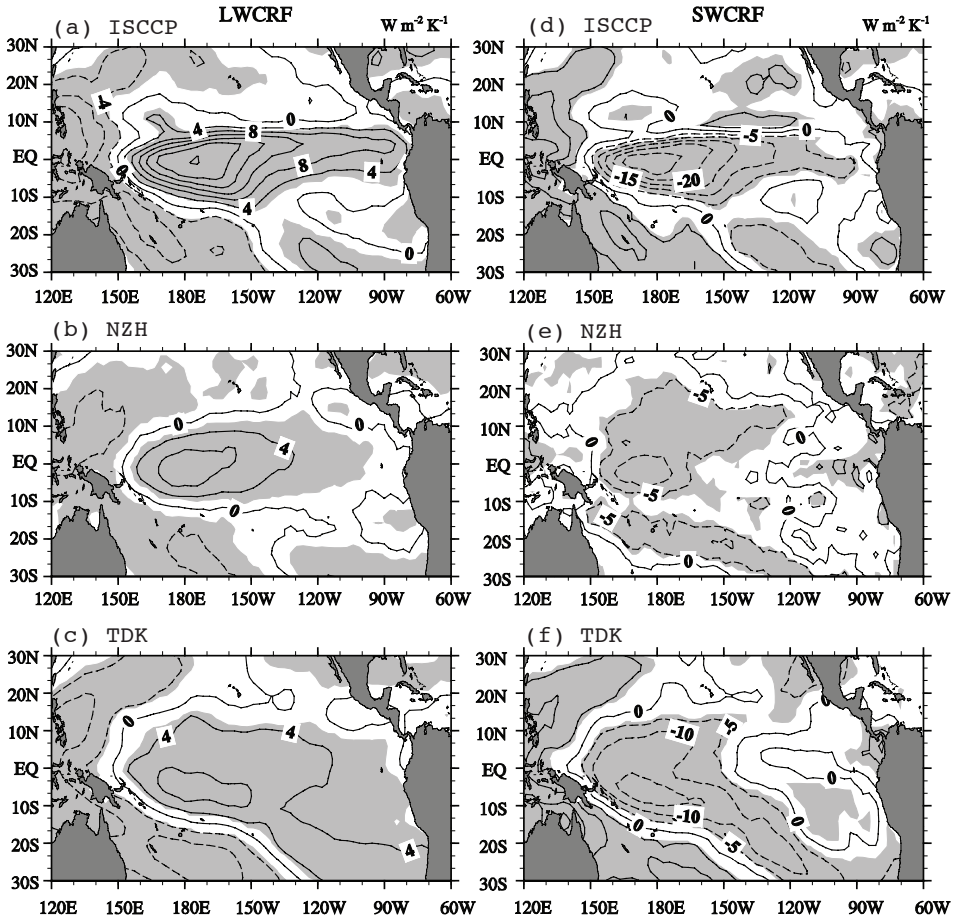

Fig. 9. As in Fig. 8 but for LWCRF (a)–(c) and SWCRF (d)–(f). The contour interval is 4 W m^{-2} K^{-1} for (a)–(c) and 5 W m^{-2} K^{-1} for (d)–(f).

clouds associated with El Niño warming (Fig. 10a). The spatial patterns of LWCRF responses are simulated well by both the NZH and TDK simulations, except with smaller magnitudes. Over the maximum response center over the central Pacific, the response coefficients are 8 W m^{-2} K^{-1} both for the NZH and TDK simulations, which is only about one third of the observed value. In addition, the simulations using NZH and TDK both miss the large value along the ITCZ region, especially over the eastern Pacific. Besides, the TDK run overestimates the positive response over the southeastern Pacific. Also, in the TDK run, the positive response over the entire region is statistically significant at the 5% level, while only over certain portions of the regions the responses are statistically significant in the ISCCP data and the NZH simulation.

Spatially, the responses of high level cloud amount mirror largely those of LWCRFs both in the ISCCP data and the two simulations (cf. Figs. 9a–9c and Figs. 10a–10c), as their spatial correlations between the responses of LWCRF and high level cloud amount all exceed 0.92. The difference in the simulated spatial patterns of the response of high level cloud amount and LWCRF suggests further evidence for the impact of convection scheme on simulated results. Note that the responses of high level cloud amount are comparable to the ISCCP data both in the NZH and TDK simulations.

The response of the cloud ice water path was also examined (Figs. 11a–11c). It can be seen that the responses of the cloud ice water path to El Niño warming in the two simulations are weaker than that in the ISCCP data. Compared to the NZH run, the response of the cloud ice water path to El Niño warming in the TDK simulation is much stronger, which is consistent with the response of LWCRF in the two simulations. This suggests that, similar to the climatology, cloud properties, such as the cloud ice water path, have a remarkable impact on the CRF in terms of magnitude.

The response of SWCRF to El Niño warming averaged over the Pacific cold tongue region in the ISCCP data is −12.28 W m^{-2} K^{-1}, while those for the NZH and TDK simulations are −4.56 and −7.08 W m^{-2} K^{-1}, respectively. This demonstrates that the

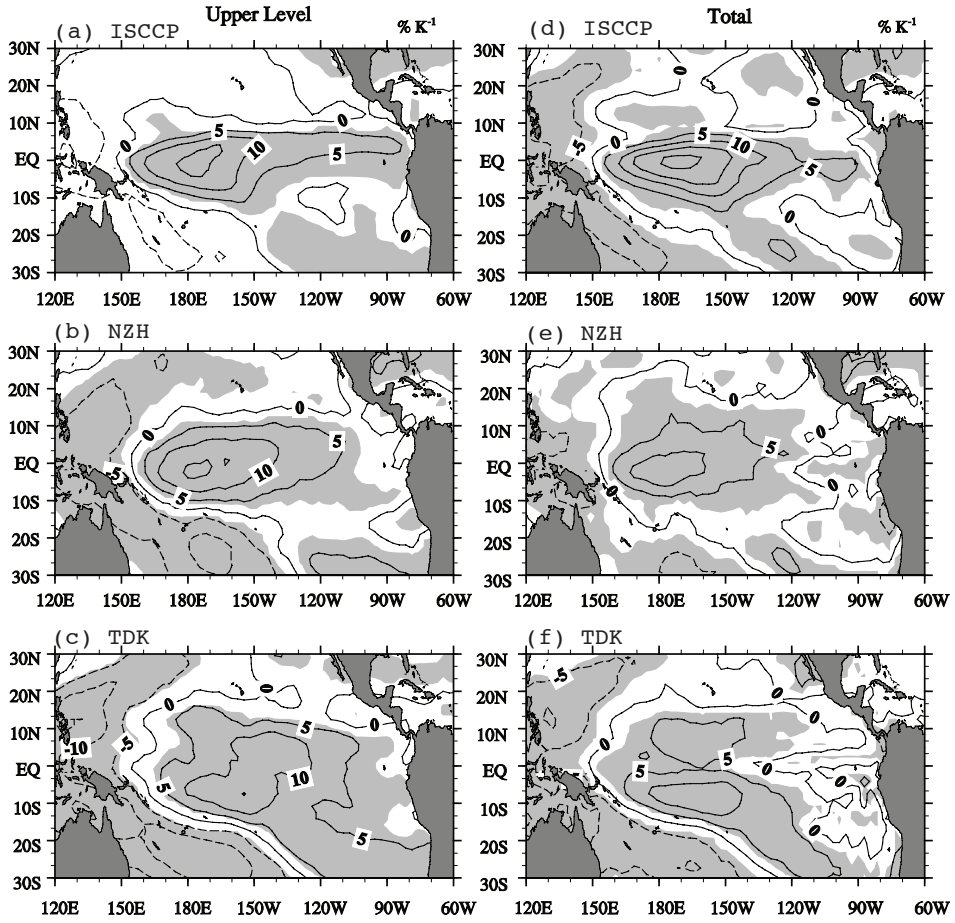

Fig. 10. As in Fig. 8 except for the upper-level cloud amount (a)–(c) and the total cloud amount (d)–(f). The contour interval is 5% K^{-1}.

responses of SWCRF are underestimated considerably in the two simulations, with the TDK simulation showing an improvement over the NZH simulation in this regard.

The geographic distributions of SWCRF response to El Niño warming are illustrated in Figs. 9d–9f. In the ISCCP data, the response of SWCRF to El Niño warming is similar to that of LWCRF in terms of spatial pattern, but of the opposite sign and with larger magnitude (Fig. 9d). The NZH run produces the negative response over the central tropical Pacific, but with smaller magnitude (Fig. 9e). In addition, the NZH run misses the positive response over the western Pacific and has a spuriously negative response extended to the central northern Pacific. In contrast, the TDK simulation represents a clear improvement over the NZH run both in spatial pattern and in magnitude of the response of SWCRF to El Niño warming. The spatial pattern of SWCRF response in the TDK simulation is similar to that of the ISCCP data, except for a missing (excessive) negative response over the eastern part of the ITCZ (the southeastern Pacific).

The spatial pattern of the response of the total cloud amount is similar to that of the SWCRF in the ISCCP data, and the responses of total cloud amounts to El Niño warming in the two simulations differ slightly from the observation data (cf. Figs. 9d–9f and Figs. 10d–10f). To a certain extent, the simulated total cloud amount responses resemble those of the SWCRF in the two simulations. In addition, there are some differences between simulated responses of total cloud amount and SWCRF. For example, in the NZH run, the significant positive response of total cloud amount along the equator extends to 120°W, while that of the SWCRF is restricted to the immediate east of the date line. Meanwhile, the TDK run produces a relatively weak positive response of total cloud amount along the equator, but the negative SWCRF response is comparable to that over the off-equatorial region.

The inconsistency between the responses of total cloud amount and SWCRF could be due to the different response patterns of the cloud water path (Figs. 11d–11f). In the NZH run, there are two large posi-

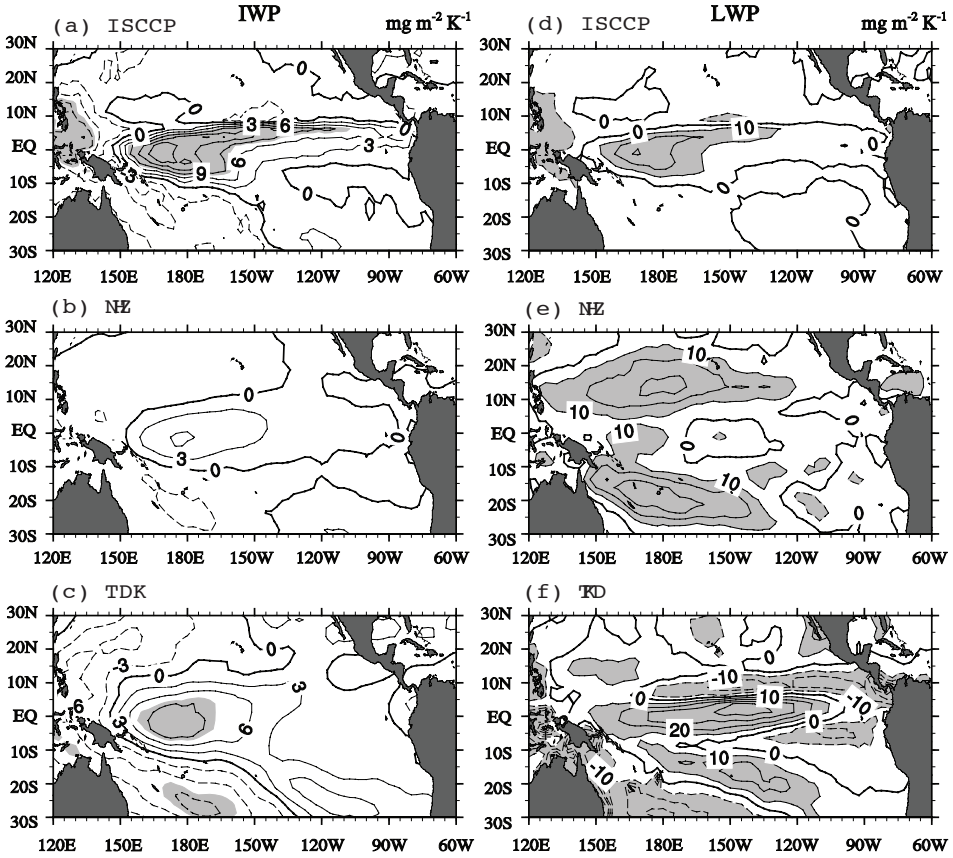

Fig. 11. As in Fig. 8 except for the cloud ice water path (a–c; IWP) and the cloud liquid water path (d–f; LWP). The regression coefficients which are statistically significant at the 5% level are shaded. The contour interval is 3 mg m^{-2} K^{-1} for IWP and 10 mg m^{-2} K^{-1} for LWP.

tive cloud water path response centers over the northwestern and southwestern Pacific and relatively small values along the equator. In contrast to the NZH simulation, the strong positive response of the cloud water path in the simulation using TDK is located along the equator. This indicates that the responses in cloud water path cause the inconsistency between the responses of total cloud amount and SWCRF near the equator, and the response of the cloud water path in the two simulations are prominently distinct.

Besides the difference in the spatial pattern, the simulations underestimate the magnitude of the response of total cloud amount over most of the domain. For instance, the responses over the maximum center are underestimated by about 5% K^{-1} by both simulations. In addition, it shows that the total cloud amount over the southeastern Pacific (30°–10°S, 150°–110°W) is overestimated by the TDK simulation. The overestimation of total cloud amount is accompanied by an excessive upper-level cloud amount and SWCRF, as well as LWCRF, indicating stronger convection. The more vigorous convection event over the southeastern Pacific is due to the lower threshold of temperature for convection to occur. To identify this threshold in the southeastern Pacific, the vertical velocity at the 500 hPa is binned as a function of SST in Fig. 12. The deep convection thresholds are close to 27.6°C and 27.1°C for the ERA40 reanalysis and NZH simulation data respectively, while for the TDK simulation it is below 26°C, which is much lower than in the reanalysis and the NZH simulation. Also, examination of the results over the Pacific cold tongue region (5°S–5°N, 170°–110°W) shows a similar result. Such a low deep convection threshold provides a loose limitation for the convection to take place over the southeastern Pacific in the TDK simulation, which could further make the responses of cloud amount and CRFs over this domain different from the ISCCP and NZH simulation data.

In Fig. 10, it can be seen that during El Niño warming, both the upper-level cloud amount and the total cloud amount increase and the magnitude of the

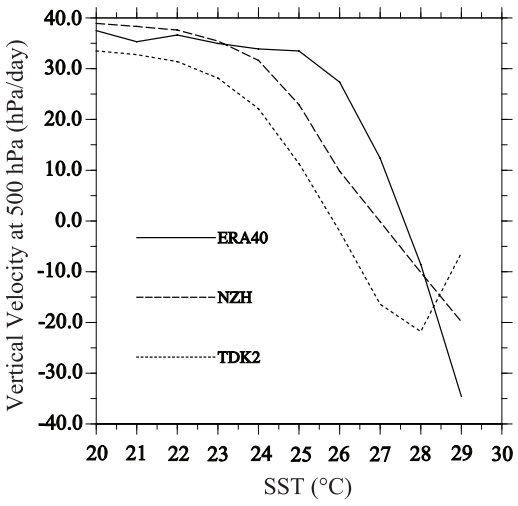

Fig. 12. Vertical velocity at 500 hPa (ω500) binned as a function of SST in the southeastern Pacific (30°–10°S, 150°–110°W): solid line for ERA40 data; dashed line for the simulation using NZH; and dotted line for the simulation using TDK. The convective threshold is defined for each curve as the limit between the subsidence regime (ω500>0) and the convective regime (ω500<0).

total cloud amount is larger than that of the upper-level cloud amount. This indicates that, besides the upper-level cloud, the middle- or lower-level cloud amount also increases during El Niño warming. But in fact, although both the upper-level and total cloud amount increase during El Niño warming, the magnitude of the former is larger than the latter both in the NZH and TDK simulation, indicating that the middle- or low-level cloud amount decreases during El Niño warming. As presenting a reasonable vertical heating and moistening profile is the classical objective of cumulus parameterization, the ability of SAMIL to produce vertical distributions of cloud warrants further investigation.

5. Summary and concluding remarks

In this study, the performances of the SAMIL model in simulating GA and CRFs have been evaluated. The impacts of the convection scheme used on the simulation of radiative forcings have been assessed. The analysis was based on the outputs of two sets of AMIP-type simulations using an identical AGCM but employing two different convection schemes: the NZH and the TDK. The major results are summarized as follows.

(1) The climatology of GA and its response to El Niño warming were reproduced well by SAMIL, both in terms of the spatial pattern and magnitude. The ultimate impacts of the convection scheme on GA were found not to be significant, due to the error compensations between water vapor and temperature.

(2) The spatial patterns of climatological LWCRF and its response to El Niño warming were reproduced reasonably by SAMIL, but with weaker magnitudes. Both the climatological spatial pattern of LWCRF and its response to El Niño were found to be sensitive to the convective scheme. The results of the NZH simulation were better than the TDK simulation for climatological LWCRF. However, the TDK simulation demonstrated an improvement over the NZH simulation for the response of LWCRF to El Niño forcing.

(3) The model showed weak performance in simulating SWCRF. A large bias was found in both spatial pattern and magnitude. The TDK scheme generally yielded better results than the NZH simulation, both in terms of climatology and the response to El Niño forcing. A spuriously excessive negative annual mean SWCRF over the southeastern Pacific and an insufficient response of SWCRF to El Niño forcing over the tropical central Pacific were seen in the NZH run. To some extent these biases were alleviated in the TDK run due to the vigorous convection over the southeastern Pacific in the TDK run. The convection activity was found to be related strongly to the low threshold for convection to occur over the Pacific.

(4) The impact of the convection scheme on the cloud profile was also found to contribute to the bias in CRFs. Analysis of the two sets of simulations revealed that during El Niño warming the increase in upper-level cloud amount was accompanied with decreases in middle- and/or lower-level cloud amount. However, in the observations, the sum of middle- and low-level cloud amount did not decrease during El Niño warming. The bias in the cloud profile could strongly influence the SWCRF.

Our analyses have indicated that the TDK convection scheme is generally better than the NZH scheme in representing tropical radiative and convection processes. However, whether this result is model-dependent requires further study. Our analysis has provided some clues for the future improvement of the LASG AGCM. For example, we found that the lower threshold of temperature for the occurrence of convection in the TDK scheme has led to model biases in the simulation of cloud and radiative forcing over the southeastern Pacific.

In this study, the radiation and cloud data from the ISCCP were taken as merits, and discrepancies were detected by comparing modeled outputs to the ISCCP data. However, the inconsistency between the ISCCP data and SAMIL results should be noted. For example, the definitions of high-level cloud amount

in the model and in the ISCCP data were found to be distinct: in the model, all cloud with a top pressure less than 440 hPa was categorized as high-level cloud, while in the ISCCP data only cloud with an optical depth larger than 0.2 and with a top pressure less than 400 hPa was detected as high-level cloud, as the threshold for cloud detection appeared to require optical depths greater than 0.2 in the ISCCP cloud algorithm (Rossow and Schiffer, 1999; Wylie and Menzel, 1999). This difference influences the high-level cloud amount significantly. Haladay and Stephens (2009) showed that the optically thin cloud, with optical depths within the range 0.02–0.3, have an approximate cloud cover in the tropical region of 30%, and that the instantaneous LWCRF of optically-thin cloud can be estimated to be -20 W m^{-2}. This is also the case for low-level cloud amount, since the thermal contrast between low-level cloud and the surface is not significant.

Also, we did not take into account the difference between the radiative transfer models used by ISCCP FD (namely, GISS 03-Model; Hansen et al., 2002) and SAMIL (namely, SES2; Sun, 2005), while the differences between these two models are significant. For example, the radiative model used by ISCCP FD has a higher spectral resolution, employing 15 noncontiguous correlated k intervals to model overlapping cloud-aerosol and gaseous absorption for the shortwave (nominally 0.2–5.0 μm) and 33 noncontiguous correlated k intervals for the longwave (nominally 5.0–200.0 μm, including one for a window wavelength of 11.1–11.3 μm) (Zhang et al., 2004), while that in SAMIL is nine for the shortwave band and eight for the longwave band, and the radiative effect of aerosol is neglected in the two simulations (Sun, 2005). In addition, in GISS 03-Model, the cloud vertical structure is derived by combining ISCCP D1 and radiosonde humidity profile observations (RAOBS) (Wang et al., 2000), while that for SES2 is the actual cloud vertical structure based on the maximum-random overlapping assumption. Further, the observed cloud optical parameters are in GISS 03-Model, while these are parameterized using the standard cloud properties parameterization schemes in SES2.

Considering all the differences between SAMIL and the ISCCP data in cloud definition and radiation calculations, it should be noted that assessments of radiative forcings at the TOA and related cloud amounts are insufficient to evaluate thoroughly the radiative process. However, it is a useful way to detect model bias and to refine models by comparing their results to observed data. New methods that favor direct comparison between modeled and observed data should be proposed and used in the future. Therefore, as a next step, it would be desirable to use the ISCCP simulator, which allows us to look into cloud properties that control radiative processes, for further assessment (Zhang et al., 2005; Wu and Zhou, 2010).

Acknowledgements. This work was supported jointly by the National Natural Science Foundation of China (Grant Nos. 40890054 and 40821092), the National Basic Research Program of China (Grant No. 2010CB951904), and National Key Technologies R&D Program (Grant No. 2007BAC29B03).

REFERENCES

Arakawa, A., 2004: The cumulus parameterization problem: Past, present, and future. *J. Climate*, **17**, 2493–2525.

Bao, Q., G. Wu, Y. Liu, J. Yang, Z. Wang, and T. Zhou, 2010: An introduction to the coupled model FGOALS1.1-s and its performance in East Asia. *Adv. Atmos. Sci.*, **27**, doi: 10.1007/s00376-010-9177-1.

Bony, S., and J. Dufresne, 2005: Marine boundary layer clouds at the heart of tropical cloud feedback uncertainties in climate models. *Geophys. Res. Lett.*, **32**, doi: 10.1029/2005GL023851.

Cess, R. D., and Coauthors, 1990: Intercomparison and interpretation of climate feedback processes in 19 atmospheric general circulation models. *J. Geophys. Res.*, **95**, 16601–16615.

Cess, R. D., and Coauthors, 1996: Cloud feedback in atmospheric general circulation models: An update. *J. Geophys. Res.*, **101**, 12791–12794.

Charlock, T. P., and V. Ramanathan, 1985: The Albedo field and cloud radiative forcing produced by a general circulation model with internally generated cloud optics. *J. Atmos. Sci.*, **42**, 1408–1429.

Chen, H., T. Zhou, R. Yu, and Q. Bao, 2009: The East Asian summer monsoon simulated by coupled model FGOALS_s. *Chinese J. Atmos. Sci.*, **33**(1), 155–167. (in Chinese)

Chen, H., T. Zhou, R. B. Neale, X. Wu, and G. J. Zhang, 2010: Performance of the New NCAR CAM3.5 in East Asian summer monsoon simulations: sensitivity to modifications of the convection scheme. *J. Climate*, **23**, 3657–3675.

Collins, W. D., and Coauthors, 2006: The Community Climate System Model version 3 (CCSM3). *J. Climate*, **19**, 2122–2143.

Colman, R., 2003: A comparison of climate feedbacks in general circulation models. *Climate Dyn.*, **20**, 865–873.

Cusack, S., A. Slingo, J. M. Edwards, and M. Wild, 1998: The radiative impact of simple aerosol climatology on the Hadley Centre climate model. *Quart. J. Roy. Meteor. Soc.*, **124**, 2517–2526.

Dai, F., R. Yu, X. Zhang, and Y. Yu, 2005: A statistically-based low-level cloud scheme and its tentative application in a general circulation model. *Acta Meteoro-*

logica Sinica, **19**, 263–274.

Del Genio, A., and W. Kovari, 2002: Climatic properties of tropical precipitating convection under varying environmental conditions. *J. Climate*, **15**, 2597–2615.

Edwards, J. M., and A. Slingo, 1996: Studies with a flexible new radiationcode. I: choosing a configuration for a large-scale model. *Quart. J. Roy. Meteor. Soc.*, **122**, 689–719.

Emanuel, K. A., and M. Zivkovic-Rothman, 1999: Development and evaluation of a convection scheme for use in climate models. *J. Atmos. Sci.*, **56**, 1766–1782.

Guilyardi, E., P. Braconnot, F. Jin, S. T. Kim, M. Kolasinski, T. Li, and I. Musat, 2009: Atmosphere feedbacks during ENSO in a coupled GCM with a modified atmospheric convection scheme. *J. Climate,* **22**, 5698–5718.

Hack, J. J., 1994: Parameterization of moist convection in the National Center for Atmospheric Research community climate model (CCM2). *J. Geophys. Res.*, **99**, 5551–5568.

Haladay, T., and G. Stephens, 2009: Characteristics of tropical thin cirrus clouds deduced from joint CloudSat and CALIPSO observations. *J. Geophys. Res.*, **114**, doi: 10.1029/2008JD010675.

Hall, A., and S. Manabe, 1999: The role of water vapor feedback in unperturbed climate variability and global warming. *J. Climate*, **12**, 2327–2346.

Hansen, J., and Coauthors, 2002: Climate forcings in Goddard Institute for Space Studies SI2000 simulations, *J. Geophys. Res.*, **107**(D18), doi: 10.1029/2001JD001143.

Hodson, D. L. R., R. T. Sutton, C. Cassou, N. Keenlyside, Y. Okumura, and T. Zhou, 2010: Climate impacts of recent multidecadal changes in Atlantic Ocean sea surface temperature: A multimodel comparison. *Climate Dyn.*, **34**, 1041–1058, doi: 10.1007/s00382-009-0571-2.

Holtslag, A. A., and C. H. Moeng, 1991: Eddy diffusivity and counter gradient transport in the convective atmospheric boundary layer. *J. Atmos. Sci.*, **48**, 1690–1698.

Houghton, J. T., Y. Ding, D. J. Griggs, M. Noguer, P. J. van der Linden, X. Dai, K. Maskell, and C. A. Johnson, 2001: *Climate change 2001: The Scientific Basis*. Cambridge University Press Cambridge, 892pp.

Hourdin, F., and Coauthors, 2006: The LMDZ4 general circulation model: Climate performance and sensitivity to parametrized physics with emphasis on tropical convection. *Climate Dyn.*, **27**, 787–813.

Klein, S. A., and D. L. Hartmann, 1993: The seasonal cycle of low stratiform clouds. *J. Climate*, **6**, 1587–1606.

Kucharski, F., and Coauthors, 2009: The CLIVAR C20C project: Skill of simulating Indian monsoon rainfall on interannual to decadal timescales. Does GHG forcing play a role? *Climate Dyn.*, **33**, 615–627, doi: 10.1007/s00382-008-0462-y.

Li, L., B. Wang, and T. Zhou, 2007, Contributions of natural and anthropogenic forcings to the summer cooling over eastern China: An AGCM study. *Geophys. Res. Lett.*, **34**, L18807, doi: 10.1029/2007GL030541

Li, J., Y. Liu, Z. Sun, and G. Wu, 2009: The impacts of the radiation and cumulus convective parameterization on the radiation fluxes in SAMIL. *Acta Meteorologica Sinica*, **67**(03), 355–369. (in Chinese)

Li, G., and G. J. Zhang, 2008: Understanding biases in shortwave cloud radiative forcing in the national center for atmospheric research community atmosphere model (CAM3) during El Niño. *J. Geophys. Res.*, **113**, doi: 10.1029/2007JD008963.

Li, H., L. Feng, and T. Zhou, 2010a: Multi-model projection of July–August climate extreme changes over China under CO_2 doubling. Part I: Precipitation. *Adv. Atmos. Sci.*, doi: 10.1007/s00376-010-0013-4.

Li, H., L. Feng, and T. Zhou, 2010b: Multi-model projection of July-August climate extreme changes over China under CO_2 doubling. Part II: Temperature. *Adv. Atmos. Sci.*, doi: 10.1007/s00376-010-0052-x.

Liu, Y. M., K. Liu, and G. X. Wu, 2007: The impacts of the cumulus convective parameterization on the atmospheric water-content and rainfall simulation in SAMIL. *Chinese J. Atmos. Sci.*, **31**, 1201–1211. (in Chinese)

Lloyd, J., E. Guilyardi, H. Weller, and J. Slingo, 2009: The role of atmosphere feedbacks during ENSO in the CMIP3 models. *Atmos. Sci. Lett.*, **10**, 170–176.

Maloney, E. D., and D. L. Hartmann, 2001: The sensitivity of intraseasonal variability in the NCAR CCM3 to changes in convective parameterization. *J. Climate*, **14**, 2015–2034.

Nordeng, T. E., 1994: Extended versions of the convective parameterization scheme at ECMWF and their impact on the mean and transient activity of the model in the tropics. ECMWF Technical Memorandum, 206, 41pp.

Ockert-Bell, M. E., and D. L. Hartmann, 1992a: The effect of cloud type on earth energy balance: Results for selected regions. *J. Climate*, **5**, 1157–1171.

Ockert-Bell, M. E., and D. L. Hartmann, 1992b: The effect of cloud type on earth-energy balance: Results for selected regions. *J. Climate*, **5**, 1157–1171.

Press, W. H., S. A. Teukolsky, W. T. Vetterling, and B. P. Flannery, 1992: *Numerical Recipes*. Cambridge University Press, 963pp.

Randall, D. A., and Coauthors, 2007: Climate models and their evaluation. *Climate Change 2007: The Physical Science Basis*, Solomon et al., Eds., Cambridge University Press, 589–662.

Raval, A., and V. Ramanathan, 1989: Observational determination of the greenhouse-effect. *Nature*, **342**, 758–761.

Rossow, W. B., and R. A. Schiffer, 1999: Advances in understanding clouds from ISCCP. *Bull. Amer. Meteor. Soc.*, **80**(11), 2261–2287.

Rossow, W. B., and E. N. Duenas, 2004: The International Satellite Cloud Climatology Project (ISCCP) Web site—An online resource for research.

Bull. Amer. Meteor. Soc., **85**, 167–172.

Sanchez-Gomez, E., C. Cassou, D. L. R. Hodson, N. Keenlyside, Y. Okumura, and T. Zhou, 2008: North Atlantic weather regimes response to Indian-western Pacific Ocean warming: A multi-model study. *Geophys. Res. Lett.*, **35**, L15706, doi: 10.1029/2008GL034345.

Scaife, A. A., Coauthors, 2009: The CLIVAR C20C Project: Selected twentieth century climate events. *Climate Dyn.*, **33**, 603–614, doi: 10.1007/s00382-008-0451-1.

Schmidt, G. A., and Coauthors, 2006: Present-day atmospheric simulations using GISS ModelE: Comparison to in situ, satellite, and reanalysis data. *J. Climate*, **19**, 153–192.

Shi, G. Y., 2007: *Atmospheric Radiation Science*. Science and Technology Press, 402pp. (in Chinese)

Shine, K. P., and A. Sinha, 1991: Sensitivity of the Earth's climate to height-dependent changes in the water vapour mixing ratio. *Nature*, **354**, 382–384.

Slingo, J. M., 1987: The development and verification of a cloud prediction scheme for the ECMWF model. *Quart. J. Roy. Meteor. Soc.*, **113**, 899–927.

Smith, T. M., and R. W. Reynolds, 2004: Improved extended reconstruction of SST (1854–1997). *J. Climate*, **17**, 2466–2477.

Soden, B. J., and I. M. Held, 2006: An assessment of climate feedbacks in coupled ocean-atmosphere models. *J. Climate*, **19**, 3354–3360.

Song, X. L., 2005: The evaluation analysis of two kinds of mass flux cumulus parameterization in climate simulation. Ph. D. dissertaion, Institute of Atmospheric Physics, Chinese Academy of Sciences, 145pp. (in Chinese)

Song, X., X. Wu, G. J. Zhang, and R. W. Arritt, 2008: Understanding the effects of convective momentum transport on climate simulations: The role of convective heating. *J. Climate*, **21**, 5034–5047.

Sun, D. Z., and R. S. Lindzen, 1993: Wator vapor feedback and the ice age snowline record. *Ann. Geophys.*, **11**, 204–215.

Sun, D. Z., J. Fasullo, T. Zhang, and A. Roubicek, 2003: On the radiative and dynamical feedbacks over the equatorial Pacific cold tongue. *J. Climate*, **16**, 2425–2432.

Sun, D. Z., and Coauthors, 2006: Radiative and dynamical feedbacks over the equatorial cold tongue: Results from nine atmospheric GCMs. *J. Climate*, **19**, 4059–4074.

Sun, Z., 2005: Parameterizations of radiation and cloud optical properties. BMRC Research Report, 1–6.

Tiedtke, M., 1989: A comprehensive mass flux scheme for cumulus parameterization in large scale models. *Mon. Wea. Rev.*, **117**, 1779–1800.

Uppala, S., 2006: From ERA-15 to ERA-40 and ERA-Interim. ECMWF–GEO Workshop on Atmospheric Reanalysis, Reading, United Kingdom, ECMWF, 17–22.

Wang, J., W. B. Rossow, and Y. C. Zhang, 2000: Cloud vertical structure and its variations from 20-yr global rawinsonde dataset. *J. Climate*, **12**, 3041–3056.

Weare, B. C., and A. M. Groups, 1996: Evaluation of the vertical structure of zonally averaged cloudiness and its variability in the atmospheric model intercomparison project. *J. Climate*, **9**, 3419–3431.

Wen, X., T. Zhou, S. Wang, B. Wang, H. Wan, and J. Li, 2007: Performance of a reconfigured Atmospheric General Circulation Model at low resolution. *Adv. Atmos. Sci.,* **24**(4), 712–728.

Wylie, D. P., and W. P. Menzel, 1999: Eight years of high cloud statistics using HIRS. *J. Climate*, **12**(1), 170–184.

Wu, C. Q., and T. J. Zhou, 2010: The cloud radiative forcing characteristics over East Asia simulated by the CFMIP Atmospheric General Circulation models. *Acta Meteorological Sinica*, in press. (in Chinese)

Xie, P., and P. A. Arkin, 1997: Global precipitation: A 17-year monthly analysis based on gauge observations, satellite estimates, and numerical model outputs. *Bull. Amer. Meteor. Soc.*, **78**(11), 2539–2558.

Xu, K. M., and D. A. Randall, 1996: A semiempirical cloudiness parameterization for use in climate models. *J. Atmos. Sci.*, **53**(21), 3084–3102.

Yu, Y., and Coauthors, 2008: Coupled model simulations of climate changes in the 20th century and beyond. *Adv. Atmos. Sci*, **25**(4), 641–654.

Zhang, G. J., 2002: Convective quasi-equilibrium in midlatitude continental environment and its effect on convective parameterization. *J. Geophys. Res.*, **107**, doi: 10.1029/2001JD001005.

Zhang, G. J., and N. A. McFarlane, 1995: Sensitivity of climate simulations to the parameterization of cumulus convection in the Canadian Climate Centre general circulation model. *Atmos.-Ocean*, **33**, 407–446.

Zhang, J., T. Zhou, Q. Bao, and B. Wu, 2010a: The vertical structures of temperature anomalies associated with El Niño simulated by LASG/IAP AGCM: Sensitivity to convection schemes. *Adv. Atmos. Sci.*, **27**, 1051–1063, doi: 10.1007/s00376-010-9167-3.

Zhang, L., T. Zhou, B. Wu, and Q. Bao, 2010b: The annual modes of tropical precipitation simulated by the LASG/IAP coupled ocean-atmosphere model FGOALS_s1.1. *Acta Meteor. Sinica*, **24**, 189–202.

Zhang, M. H., W. Y. Lin, S. A. Klein, J. T. Bacmeister, S. Bony, R. T. Cederwall, and A. D. D. Genio, 2005: Comparing clouds and their seasonal variations in 10 atmospheric general circulation models with satellite measurements. *J. Geophys. Res.*, **110**, doi: 10.1029/2004JD005021.

Zhang, T., and D. Z. Sun, 2006: Response of water vapor and clouds to El Niño warming in three NCAR models. *J. Geophys. Res.*, **111**, doi: 10.1029/2005JD006700.

Zhang, T., and D. Sun, 2008: What causes the excessive response of clear-sky greenhouse effect to El Niño warming in NCAR Community Atmosphere Models? *J. Geophys. Res.*, **113**, doi: 10.1029/2007JD009247.

Zhang, Y., W. B. Rossow, A. A. Lacis, V. Oinasm, and M.

I. Mishchenko, 2004: Calculation of radiative fluxes from the surface to top of atmosphere based on ISCCP and other global data sets: Refinements of the radiative transfer model and the input data. *J. Geophys. Res.*, **109**, doi: 1029/2003JD004457.

Zhou, T., and Z. Li, 2002: Simulation of the east Asian summer monsoon by using a variable resolution atmospheric GCM. *Climate Dynamics*, **19**, 167–180

Zhou, T., and R. Yu, 2006: Twentieth century surface air temperature over China and the globe simulated by coupled climate models. *J. Climate*, **19**, 5843–5858.

Zhou, T., R. Yu, X. Liu, Y. Guo, Y. Yu, and X. Zhang, 2005a: Weak response of the Atlantic thermohaline circulation to an increase of atmospheric carbon dioxide in IAP/LASG Climate System Model. *Chinese Science Bulletin*, **50**(6), 592–598.

Zhou, T., R. Yu, Z. Z. Wang, and T. W. Wu, 2005b: *The Atmospheric General Circulation Model SAMIL and Its Associated Coupled Climate System Model FGOALS-s*. Vol. 4, *Impacts of the Ocaen-Land-Atmosphere Interaction over the Asian Monsoon Domain on the Climate Change over China*, China Meteorological Press, 288pp. (in Chinese)

Zhou, T., Y. Yu, H. Liu, W. Li, X. You, and G. Zhou, 2007: Progress in the development and application of climate ocean models and ocean-atmosphere coupled models in China. *Adv. Atmos. Sci.*, **24**(4), 729–738.

Zhou, T., B. Wu, X. Wen, L. Li, and B. Wang, 2008: A fast version of LASG/IAP climate system model and its 1000-year control integration. *Adv. Atmos. Sci.,* **25**(4), 655–672, doi: 10.1007/s00376-008-0655-7.30.

Zhou, T., B. Wu, and B. Wang, 2009a: How well do Atmospheric General Circulation Models capture the leading modes of the interannual variability of Asian-Australian Monsoon? *J. Climate*, **22**, 1159–1173.

Zhou, T., and Coauthors, 2009b: Why the western pacific subtropical high has extended westward since the late 1970s. *J. Climate*, **22**, 2199–2215.

Zhou, T., and Coauthors, 2009c: The CLIVAR C20C Project: Which components of the Asian-Australian Monsoon circulation variations are forced and reproducible? *Climate Dyn.*, **33**, 1051–1068, doi: 10.1007/s00382-008-0501-8.